Research Article Vol. 40, No. 7 / July 2023 / Journal of the Optical Society of America A 1409

Journal of the Optical Society of America A

OPTICS, IMAGE SCIENCE, AND VISION

Super-resolution computational saturated absorption microscopy

Gabe Murray,[1] Patrick A. Stockton,[2] Jeff Field,[2,3] Ali Pezeshki,[2,4] Jeff Squier,[5] and Randy A. Bartels[2,6,*]

[1]Department of Physics, Colorado State University, Fort Collins, Colorado 80523, USA
[2]Department of Electrical and Computer Engineering, Colorado State University, Fort Collins, Colorado 80523, USA
[3]Center for Imaging and Surface Science, Colorado State University, Fort Collins, Colorado 80523, USA
[4]Department of Mathematics, Colorado State University, Fort Collins, Colorado 80523, USA
[5]Department of Physics, Colorado School of Mines, Golden, Colorado 80401, USA
[6]School of Biomedical Engineering, Colorado State University, Fort Collins, Colorado 80523, USA
*randy.bartels@colostate.edu

Received 23 January 2023; revised 26 May 2023; accepted 30 May 2023; posted 31 May 2023; published 23 June 2023

Imaging beyond the diffraction limit barrier has attracted wide attention due to the ability to resolve previously hidden image features. Of the various super-resolution microscopy techniques available, a particularly simple method called saturated excitation microscopy (SAX) requires only simple modification of a laser scanning microscope: The illumination beam power is sinusoidally modulated and driven into saturation. SAX images are extracted from the harmonics of the modulation frequency and exhibit improved spatial resolution. Unfortunately, this elegant strategy is hindered by the incursion of shot noise that prevents high-resolution imaging in many realistic scenarios. Here, we demonstrate a technique for super-resolution imaging that we call computational saturated absorption (CSA) in which a joint deconvolution is applied to a set of images with diversity in spatial frequency support among the point spread functions (PSFs) used in the image formation with saturated laser scanning fluorescence microscopy. CSA microscopy allows access to the high spatial frequency diversity in a set of saturated effective PSFs, while avoiding image degradation from shot noise.

https://doi.org/10.1364/JOSAA.482203

1. INTRODUCTION

Optical imaging is a pervasive tool used to observe the world because the optical radiation can nondestructively interrogate complex objects to perform a wide array of useful tasks. Conventional imaging strategies are limited in their ability to resolve fine spatial features due to what was previously viewed as a fundamental limitation on the ability to resolve features significantly smaller than the optical wavelength [1]. This limitation stems from the fact that only spatial frequencies smaller than the optical wavelength will propagate any reasonable distance for far-field detection. As a result, the high spatial frequency content obtained through interaction with objects containing structures much smaller than the wavelength evanescently decays, which leads to a long-held notion that imaging such small features requires a near-field scanning method [2] to optically image such small object features.

The emergence of super-resolution imaging techniques has shattered the notion that sub-wavelength structures cannot be resolved with far-field optical microscopy [3–5]. Through the manipulation of excited state populations with nonlinear switching beams, the region of luminescent emission [6,7] or transient absorption [8] can be restricted to a region an order of magnitude smaller than a diffraction-limited focal spot. These methods require the careful overlap of two laser beams of different colors: an excitation beam and a de-excitation beam.

An alternate method that exploits a simpler experimental strategy only requires a single beam to drive the excited state population into saturation. This method, called saturated excitation (SAX) microscopy [9,10], can produce images that resolve spatial features with a resolution that defeats the diffraction limit. SAX super-resolution images are obtained by modulating the total power of the illumination light intensity sinusoidally and measuring the harmonics of the input modulation frequency recovered from the signal emitted by the object. While SAX microscopy is an elegant laser scanning method that requires only a small modification of a laser scanning microscope, SAX enhancements in resolution improvement suffer from contamination by the shot noise that is present across all harmonics [11]. A further improvement to this method called dSAX [10] extracts the nonlinear signal in a more efficient manner, yielding the same resolution enhancements as SAX, but with a higher SNR. While this method improves the SNR, it still discards most of the energy contained in the signal by separating

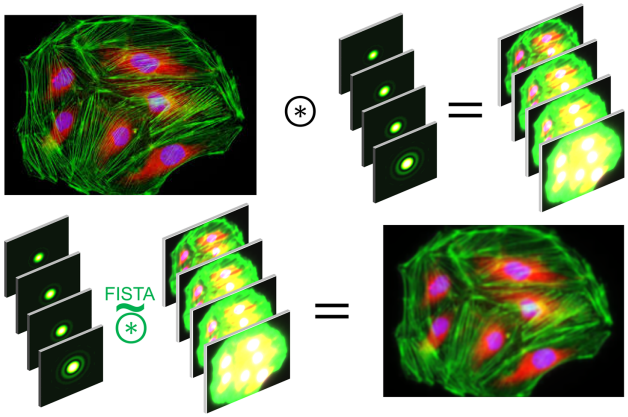

Fig. 1. Graphical representation of how the data (top) and image (bottom) are formed using CSA (excluding noise). Image courtesy of MicroscopyU [13].

the higher-resolution images according to different orders of nonlinear signal extracted.

In this paper, we demonstrate what we believe, to the best of our knowledge, is a new technique called computational saturated absorption (CSA) using a joint deconvolution fusion algorithm called super-deconvolution imaging (SDI) [12]. CSA produces excellent super-resolution image quality under conditions where SAX imaging is highly degraded due to corruption by shot noise. In our improved imaging approach, a sequence of laser-scanned fluorescent images are acquired under differing levels of saturation of the excited state of the fluorescent molecule. The underlying object is estimated from the set of images that are jointly deconvolved with the set of saturated point spread functions (PSFs), as shown in Fig. 1. The power of the CSA technique is that it does not rely on information only contained at a certain harmonic to get super-resolution information and is able to use all the nonlinear components together instead of separately. CSA leverages prior information of the saturation function and iteratively solves for an image that best matches the entire set of data given the model of how the PSF should change with corresponding levels of saturation. This leads to a high-resolution, high-SNR image without the need to trim out certain portions of the signal that contain the nonlinear response, as in SAX and dSAX. At higher levels of saturation, the effective PSF (ePSF) becomes brighter, broader, and steeper, so that the SNR of the data and the steepness of the edges of the ePSF increase. With this strategy, we obtained higher-resolution images than allowed by the diffraction limit. Moreover, we show that the image quality obtained by CSA is superior to imaging under similar conditions with SAX microscopy as well as traditional deconvolution techniques.

2. THEORY

To appreciate the improvements in super-resolution imaging through CSA over SAX, we considered the effect of the PSF saturation in the two methods. In both cases, we modeled a laser beam focused to a diffraction-limited spot that can be described by the PSF for unaberrated illumination optics as $\mathrm{PSF}_i(\tilde{\rho}) = J_1(2\pi \mathrm{NA}_i \tilde{\rho})/(\pi \mathrm{NA}_i \tilde{\rho})$. The numerical aperture (NA) of the illumination optic is NA_i and $\tilde{\rho}$ is the radial spatial coordinate $\boldsymbol{\rho}$ that is normalized by the excitation wavelength λ and J_1 is a first-order Bessel function of the first kind. In both CSA and SAX, the illumination beam is used to drive a fluorescent molecule into saturation during excitation. Assuming a three-level molecular system with a cw excitation model, the excited state population is given by $e(\tilde{\rho}) = \alpha(\tilde{\rho})/(1+\alpha(\tilde{\rho}))$. The local saturation is $\alpha(\tilde{\rho}) = \alpha_0 \mathrm{PSF}_i(\tilde{\rho})$, with the peak saturation value $\alpha_0 = I_0/I_{\mathrm{sat}}$ defined as the ratio of the peak illumination intensity I_0 to the saturation intensity of the fluorophore I_{sat}.

The traditional SAX method for image formation uses information contained in harmonics generated from the nonlinear response of the saturation excitation of the sample. SAX microscopy exploits a sinusoidal temporal modulation of the illumination beam of the form $\alpha(\tilde{\rho})\, f_m(x)$, where the temporal modulation is of the form $f_m(x) = (1+\cos(x))/2$, $x = \omega_m t$, and ω_m is the input modulation frequency. Temporal modulation of the local saturation produces an excited state population that varies in space and time, so $e_s[\alpha(\tilde{\rho}), x] = \alpha(\tilde{\rho})\, f_m(x)/[1+\alpha(\tilde{\rho})\, f_m(x)]$. The nonlinear functional mapping imparted by the nonlinear saturated excitation function produces harmonics $q\omega_m$, where q is the harmonic order index. Each harmonic separately yields an image, which contains resolution information beyond that of the diffraction limit. With each increasing harmonic, the resolution improves, but the SNR drops dramatically. The imaging model for SAX is generally constructed by considering a Taylor series expansion of the excited state saturation, which generates harmonics of the input modulation frequency ω_m that lead to an impulse response for harmonics that geometrically scale the harmonic order; i.e., $\mathrm{PSF}_q(\tilde{\rho}) \propto \mathrm{PSF}_i^q(\tilde{\rho})$. Unfortunately, the Taylor expansion diverges for relatively small values of peak saturation ($\alpha_0 \sim 0.4$), yet large values of peak saturation are required to produce appreciable SNR in SAX images. The limitation of the Taylor expansion is easily remedied by computing a cosine series expansion amplitude of the excited state population at the q^{th} harmonic of the saturated excited state population $c_q(\alpha) = (2\pi)^{-1} \int_{-\pi}^{\pi} e_s(\alpha, x) \cos(qx)\mathrm{d}x$. An analytic solution $c_q(\alpha) = (\alpha/2)_2 \tilde{F}_3(1, 3/2, 2; 2-q, 2+q; -\alpha)$ is expressed in terms of a regularized hypergeometric function ${}_2\tilde{F}_3$. The PSF for the q^{th} SAX order follows from the expansion coefficient $\mathrm{PSF}_q(\tilde{\rho}) = c_q[\alpha_0 \mathrm{PSF}_i(\tilde{\rho})]$.

To estimate the SNR, consider a set of N fluorophores with a radiative emission rate of k_r that are localized to a subresolution region in space. The maximum signal for the q^{th} SAX order occurs when the peak of the illumination PSF is centered on the fluorescent probe, resulting in a detected photo rate $\phi_q = \eta_D N k_r c_q(\alpha_0)$ that depends on the level of saturation. SAX signals are subject to multiplexed noise because they are detected in the frequency domain, which means that the shot noise is determined by the average detected photon emission rate that is given by $\phi_0 = \eta_D N k_r c_0(\alpha_0)$, where $c_0(\alpha) = 1-(1+\alpha)^{(-1/2)}$, indicating that shot noise rises with increasing saturation. Here, η_D represents the total detection efficiency, including the detector efficiency, the transmission efficiency through optical components, and the collection efficiency of the objective The peak SNR for the q^{th} order SAX image is $\mathrm{SNR}_q = \kappa_q \mathrm{Y}$. Here, $\kappa_q = c_q(\alpha_0)/\sqrt{c_0(\alpha_0)}$ and

$\Upsilon = \sqrt{N k_r \eta_D \Delta t}$, with Δt denoting the observation time. For a ∼100 nm diameter sphere with a fluorescent dye and typical numbers of $N \sim 1000$, $k_r \sim 1/3.8$ ns, $\eta_D \sim 0.1$, and $\Delta t = 50$ µs, then $\Upsilon \sim 1000$. For a peak saturation parameter of $\alpha_0 = 0.4$, then $\kappa_1 = 0.18$, $\kappa_2 = 0.015$, $\kappa_3 = 0.0013$, $\kappa_4 = 1.1 \times 10^{-4}$. Thus, for these numbers, only the first three harmonic orders will rise above the noise threshold even in the shot noise limit. Higher saturation is required to obtain higher harmonics; however, the PSF for the harmonics will broaden at increased saturation, degrading the improvements in spatial resolution.

In contrast, the CSA imaging demonstrated here can exploit the high spatial frequency content probed by driving laser scanning microscopy (LSM) into saturation, while simultaneously improving the SNR as higher-resolution imaging is scaled with increased peak saturation. In CSA, we recorded a set of LSM images, each with an increased level of peak saturation of the illumination PSF. A primary CSA advantage is that the signal at each saturation level is obtained directly from the saturated excitation level, leading to an ePSF given by $\psi(\tilde{\rho}) = (\alpha_0 \mathrm{PSF}_i(\tilde{\rho}))/(1 + \alpha_0 \mathrm{PSF}_i(\tilde{\rho}))$ that is parameterized by the peak saturation parameter α_0. Because CSA does not suffer from excess background signal levels, the SNR coefficient for the recorded image at each saturation level is simply determined by the detected fluorescent photons from the peak of the PSF at $\tilde{\rho} = 0$, leading to a value $\kappa_{\mathrm{CSA}} = \sqrt{\alpha_0/(1+\alpha_0)}$. Several ePSFs for a range of α_0 values are shown in Fig. 2(d).

3. JOINT DECONVOLUTION ALGORITHM

CSA jointly exploits the information gained by probing a sample with a set of saturated effective PSFs at several saturation levels. For each image, the incident laser power is adjusted to set the peak saturation $\alpha_{0,s}$ that produces an image with an effective saturated PSF that we denote as $\psi_s(\boldsymbol{\rho})$, and the subscript s labels the image in the set with the corresponding saturation level $\alpha_{0,s}$, which goes from 1 to M. The 2D discrete approximation to the ePSF is indicated by the ePSF in bold; $\boldsymbol{\psi}_s = \psi_s(x_i, y_j)$

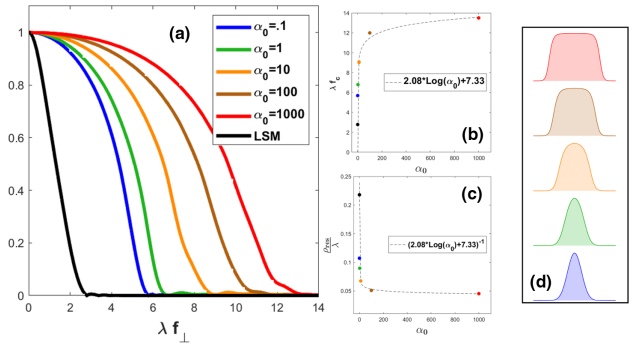

Fig. 2. (a) Expected MTF to increase the levels of saturation in the asymptotic limit. (b) and (c) How the expected resolution trends with the max saturation level. (a)–(c) Normalized in terms of wavelength so they are all unitless. (d) Illustration of how the PSF changes shape according to the maximum saturation level of each simulation. Each MTF is generated using the CSA technique with a set of 15 PSFs evenly sampling the saturation curve starting from $.01 I_{\mathrm{sat}}$ to the maximum saturation level. The plots to the right show the PSFs at increasing levels of peak saturation ($\alpha_0 = I_0/I_{\mathrm{sat}} = [.1, 1, 10, 100, 1000]$, respectively).

and x_i and y_j are discrete spatial coordinates values. The computational algorithm uses a vector form of the discrete ePSF $\vec{\boldsymbol{\psi}}_s = [\boldsymbol{\psi}_s]_{\mathrm{flatten}}$, in which the flattened vector is composed of the columns of $\boldsymbol{\psi}_s$ stacked on top of one another.

For a fluorescent object with a spatial distribution of fluorophore concentration $c(\boldsymbol{\rho})$, a recorded image in the set is proportional to $c(\boldsymbol{\rho}) \circledast \psi_s(\boldsymbol{\rho})$ as with any incoherent LSM technique. The discrete approximation to the convolution model can be written as a matrix equation $\vec{\mathbf{y}}_s = \mathbf{A}_s \vec{\mathbf{c}} + \vec{\mathbf{n}}_s$; that is, the discrete 2D convolution between $\boldsymbol{\psi}_s$ and the discrete object $[\boldsymbol{c}]_{i,j} = c(x_i, y_j)$ flattened to a column vector $\vec{\boldsymbol{c}} = [\boldsymbol{c}]_{\mathrm{flatten}}$. The convolution measurement matrix operator $\mathbf{A}_s$ is the matrix form of the discrete convolution integral for an ePSF $\boldsymbol{\psi}_s$. Each row of this matrix represents a shifted version of $\vec{\boldsymbol{\psi}}_s$. The discrete signal vector $\vec{\mathbf{y}}_s$ is a 2D image that has been flattened into a vector. Noise in the measurement is denoted by $\vec{\mathbf{n}}_s$.

The effective optical transfer function (eOTF) is given by $\Psi_s(k_x, k_y) = \mathscr{F}\{\psi_s(\boldsymbol{\rho})\}$, where $\mathbf{k}_\perp = (k_x, k_y)$ is the conjugate variable to $\boldsymbol{\rho}$ and $\mathscr{F}\{\}$ is a Fourier transform. The vectorized eOTF $\vec{\boldsymbol{\Psi}}_s = [\boldsymbol{\Psi}_s]_{\mathrm{flatten}}$ is the flattened form of the discrete eOTF $\boldsymbol{\Psi}_s$. Because the image formation process for the saturated ePSF is linear and shift invariant, the convolution operator has the form $\mathbf{A}_s = \mathbf{F}^\dagger \mathrm{diag}\{\vec{\boldsymbol{\Psi}}_s\}\mathbf{F}$, with discrete Fourier transform (DFT) and the DFT adjoint operators denoted by $\mathbf{F}$ and $\mathbf{F}^\dagger$, respectively. As the convolution operator is diagonalized by the DFT, the adjoint of the convolution operator is simply $\mathbf{A}_s^\dagger = \mathbf{F}^\dagger \mathrm{diag}\{\vec{\boldsymbol{\Psi}}_s\}^* \mathbf{F}$, where * represents the complex conjugate. The fact that the adjoint operator is equivalent to a cross correlation is exploited to construct a computationally efficient CSA image estimation algorithm. The signal spatial frequency vector is thus given by $\vec{\mathbf{Y}}_s = \vec{\boldsymbol{\Psi}}_s \circ \vec{\mathbf{C}} + \vec{\mathbf{N}}_s$, where $\circ$ denotes an element-wise (Hadamard) product between the vectors. Here, $\vec{\mathbf{C}} = \mathbf{F}\vec{\mathbf{c}}$, $\vec{\mathbf{Y}}_s = \mathbf{F}\vec{\mathbf{y}}$, and $\vec{\mathbf{N}}_s = \mathbf{F}\vec{\mathbf{n}}_s$ are the spatial frequency vectors of the object, signal, and noise, respectively.

CSA employs a set of data vectors, each taken at a distinct level of peak saturation $\alpha_{0,s}$, from which the underlying object $\vec{\boldsymbol{c}}$ is jointly estimated. In the simplest form, we seek to find an optimal object vector $\vec{\boldsymbol{c}}^*$ by

$$\vec{\boldsymbol{c}}^* := \underset{\vec{\boldsymbol{c}}>0}{\mathrm{argmin}} \frac{1}{2} \left(\left\| \mathbf{A}_T \vec{\boldsymbol{c}} - \vec{\boldsymbol{y}}_T \right\|_2 + \left\| \lambda I \vec{\boldsymbol{c}} \right\|_2 \right), \qquad (1)$$

which is a problem formulated as a least mean squared fit. Here, both the total signal vector $\vec{\boldsymbol{y}}_T$ and the convolution operator $\mathbf{A}_T$ are concatenations of the full data set of M independent images at separate saturation levels, as shown in Figs. S2 and S3; therefore, for an $N \times N$ data scan for each image, each signal vector of length N^2 is concatenated to form $\vec{\mathbf{y}}_T$ of length MN^2. Similarly, $\mathbf{A}_T$ is a tall and skinny matrix with dimensions of $MN^2 \times N^2$; each $\mathbf{A}_s$ is stacked on top of one another vertically, as shown in Fig. S2. To illustrate the CSA principle and to estimate the PSF and OTF of the result of super deconvolution, we compute Eq. (1), with a very small λ value, which avoids large values in the reconstruction due to small eigenvalues of $\mathbf{A}_T^\dagger \mathbf{A}_T$. We directly obtain the LMS solution by computing the regularized Moore–Penrose pseudoinverse of the concatenated data and convolution operators, which yields

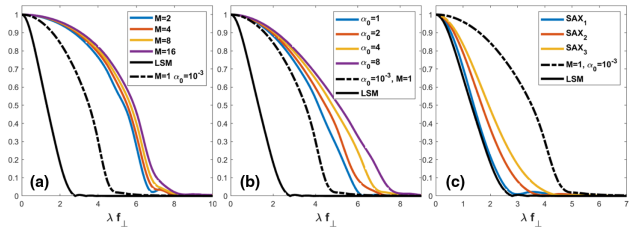

Fig. 3. These plots show the simulated MTF by direct computation using the pseudoinverse. A point object was reconstructed, which was much narrower than the simulated PSFs. The Fourier transform of the reconstruction was then taken to produce the MTFs. A computing cluster (ASHA) with 192 GB RAM was used to carry out these simulations. (a) Corresponding MTF for increasing the number of PSFs used in the super deconvolution for the saturation intensity increasing from $.1\,I_{\text{sat}}$ to $4\,I_{\text{sat}}$. The dashed line corresponds to the usual deconvolution using a single PSF with the intensity set to $.001\,I_{\text{sat}}$. The solid black line is the MTF for the laser scanned image without deconvolution. (b) Illustration of how the MTF changes with increasing the maximum intensity to different multiples of I_{sat} ($\alpha_0 = \frac{I_0}{I_{\text{sat}}}$). Each colored curve is the result of the super deconvolution using 15 PSFs rising to the corresponding saturation level. The dashed line is again the deconvolution with a single unsaturated PSF. (c) Comparison of MTFs generated with the traditional SAX technique using the same illumination PSF and a saturation level of $\alpha_0 = 4$. The first, second, and third harmonics are used to generate the MTFs. In all the plots, the axis is normalized in terms of wavelength and spatial frequency to be unitless. All three simulations used an illumination wavelength of $\lambda = 500$ nm with an NA = 1.4 objective to set the initial resolution.

the solution $\vec{\boldsymbol{c}}^{*} = (\mathbf{A}_T^{\dagger}\mathbf{A}_T + \lambda I)^{-1}\mathbf{A}_T^{\dagger}\vec{\boldsymbol{y}}_T$, where $^{-1}$ indicates the matrix inverse. The results of noise-free simulations of a sub-resolution point object to estimate the PSF and OTF are presented in Fig. 3. Even in a noise-free case, CSA outperforms both a simple linear devolution and conventional SAX imaging by providing much better spatial frequency support for image formation. Asymptotic behavior of the OTFs with very high levels of saturation is further explored in Fig. 2.

Computation of the pseudoinverse provides a direct solution to the super-deconvolution problem for CSA but is infeasible for realistic image sizes. For an image size of 256×256 and a set of 15 images (each at a different saturation level) with zero padding, the matrix occupies ~512 GB of data, which exceeds the available memory in most computers. This computational hurdle can be significantly reduced by carrying out the operation of $\mathbf{A}_T$ and $\mathbf{A}_T^{\dagger}$ equivalently in terms of Fourier transforms, which eliminates the need to store a large concatenated Toeplitz matrix $\mathbf{A}_T$ in memory. Due to computational constraints, we solved the CSA problem with an iterative optimization algorithm called the fast iterative shrinkage thresholding algorithm (FISTA). Because FISTA is a regularized form of a gradient descent optimization algorithm we needed a current guess and the gradient of Eq. (1). The key to handling large data sets with such an algorithm is to find a method to compute the gradient value for each iteration without requiring instantiating $\mathbf{A}_T$ [14].

For efficient computation, the gradient term in the FISTA algorithm is computed without inverting and instantiating the large matrices that arise in the CSA problem. To do so, the gradient $\vec{\mathbf{g}}$ of Eq. (1), which for a single image deconvolution is given by $\vec{\mathbf{g}}_s = \mathbf{A}_s^{\dagger}(\mathbf{A}_s[\vec{\boldsymbol{c}} - \vec{\mathbf{y}}_s]) + \lambda^2\vec{\boldsymbol{c}}$, is computed through FFT operations with $\vec{\mathbf{g}}_s = \mathbf{F}^{\dagger}(\vec{\boldsymbol{\Psi}}_s^{*} \circ \mathbf{F}[\mathbf{F}^{\dagger}(\vec{\boldsymbol{\Psi}}_s \circ \vec{\mathbf{C}})] - \vec{\mathbf{y}}_s)$. As shown in Supplement 1, the efficient gradient computation can be extended to the concatenated set of saturated measurements by looking closely at the operation of the joint convolution operator $\mathbf{A}_T$ and its adjoint $\mathbf{A}_T^{\dagger}$ and comparing to the calculation of the convolution and cross correlation using Fourier transforms. The convolution of the concatenated set of progressively saturated ePSFs $\boldsymbol{\psi}_T$ and the concentration map of our image $\boldsymbol{c}$ can be calculated $\boldsymbol{\psi}_T \circledast \boldsymbol{c} = \mathbf{F}^{\dagger}(\mathbf{F}\boldsymbol{\psi}_T \circ \mathbf{Fpad}[\boldsymbol{c}])$. The $\mathbf{pad}(\,)$ operation zeropads the object $\boldsymbol{c}$ so it becomes the same size as ψ_T (ψ_T is $MN \times N$ and $\boldsymbol{c}$ is $N \times N$). The padding operation allows the Hadamard product to be carried out and gives the same result as $\mathbf{A}_T\vec{\boldsymbol{c}}$ after being flattened. The adjoint operation $\mathbf{A}_T^{\dagger}$ operates on an array that is the same size as our data vector $\vec{\boldsymbol{y}}_T$ and outputs a vector the size of $\vec{\boldsymbol{c}}$.

The adjoint of a convolution is a cross correlation that can be calculated using Fourier transforms as $\psi_T \star \mathbf{v}_T = \mathbf{F}^{\dagger}(\mathbf{F}\boldsymbol{\psi}_T^{*} \circ \mathbf{F}\mathbf{v}_T)$, where $\star$ represents the cross correlation and $\mathbf{v}$ is a dummy array the same size as ψ_T. The problem here is that the output of this calculation is not the same size as $\mathbf{A}_T^{\dagger}\mathbf{v}_T$. This discrepancy is due to the limited number of columns of $\mathbf{A}_T$. The operation of $\mathbf{A}_T^{\dagger}$ only has enough rows to shift ψ_T with respect to $\mathbf{v}_T$ one image width when carrying out the cross correlation. As shown in Supplement 1, this means the $\mathbf{A}_T^{\dagger}$ operation only returns the central part of the cross correlation of the concatenated arrays, which is equivalent to $\sum_{s=1}^{M} \psi_s \star \mathbf{v}_s$. The full cross correlation returns the concatenation of the sum of different combinations of images in the set given as $\mathbf{F}^{\dagger}(\mathbf{F}\boldsymbol{\psi}_T^{*} \circ \mathbf{F}\mathbf{v}_T) = [\psi_1 \star \mathbf{v}_1 | \sum_{j=1}^{2} \psi_j \star \mathbf{v}_j | \sum_{j=1}^{3} \psi_j \star \mathbf{v}_j | \sum_{j=2}^{3} \psi_j \star \mathbf{v}_j | \psi_3 \star \mathbf{v}_3]$ (for $M = 3$). The required adjoint is contained only in the central image of this full cross correlation.

We can now calculate the operation of $\mathbf{A}_T$ and $\mathbf{A}_T^{\dagger}$ using efficient FFTs without holding $\mathbf{A}_T$ in memory using $\mathbf{A}_T\vec{\boldsymbol{c}} = [\mathbf{F}^{\dagger}(\boldsymbol{\Psi}_T \circ \mathbf{Fpad}[\boldsymbol{c}])]_{\text{flatten}}$ and $\mathbf{A}_T^{\dagger}\vec{\boldsymbol{v}}_T = [C(\boldsymbol{\Psi}_T^{*} \circ \mathbf{F}\mathbf{v}_T)]_{\text{flatten}}$. Here, $C(\cdot)$ is a cropping operator that denotes taking the central part of the array and $[\cdot]_{\text{flatten}}$ describes taking the 2D array and flattening it into a vector. Using this description, we can now carry out the super deconvolution of the set of data and saturated PSFs using FISTA while avoiding storing large matrices in memory. Typical run times to perform the joint deconvolution range from 5 to 15 min depending on the size of the data and the required number of iterations. This produces a single image that combines information from each LSM image to synthesize a high SNR super-resolution image. See Supplement 1 for a comprehensive overview and detailed explanation of the CSA algorithm. The pseudocode for the algorithm is shown in algorithm S2 in Supplement 1 and a block diagram is shown in Fig. 4.

4. RESULTS

To benchmark the expected performance of the CSA algorithm, we performed simulations, the results of which are shown in Fig. 5. As discussed earlier, CSA can fully exploit the improved high spatial frequency object information because this strategy does not suffer from multiplexed shot noise that buries the higher harmonics in traditional SAX imaging. The top left set of images in Fig. 5 displays the results of our simulations, where the

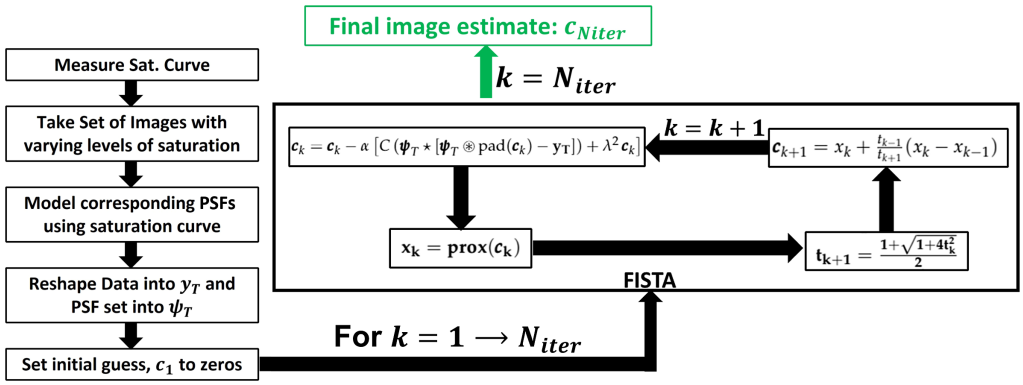

Fig. 4. Block diagram showing each step of CSA imaging as well as the FISTA algorithm.

left column shows dSAX with and without noise, as shown in Figs. 5(d) and 5(a), respectively. The middle column of images are traditional third-order ($q = 3$) SAX images (noise-free), as shown in Fig. 5(b), and with noise, as shown in Fig. 5(e). The right column has images for CSA, with Fig. 4(c) showing the noise-free result and Fig. 5(f) showing the result when noise is present. While the images in the bottom row are degraded compared to the top row, CSA super-resolution imaging is significantly more robust to noise and produces a much higher-quality image. As shown in Fig. 3(a), the number of PSFs used does not show a dramatic difference in OTF support. Fifteen PSFs were used in the simulations, but similar results should be expected to use fewer PSFs. While the superior image quality is evident in Fig. 5(f), the image itself provides no quantitative argument for the superior image quality.

To evaluate the spatial frequency information content of the reconstructed images, the radially averaged spatial frequency content of the images is shown in Fig. 5(g). The true object radial spatial frequency distribution is denoted by the solid black line. Noise-free reconstructions for a maximum peak saturation parameter of $\alpha_0 = 4$ are shown by solid lines for dSAX, CSA, and three harmonics of SAX. Image reconstructions in the presence of both additive Gaussian (standard deviation of 1% of the maximum value) and Poisson noise (mean photon count = 25000) are indicated by dashed lines of the same color. CSA shows robust behavior in the presence of noise, whereas the limitations of the multiplexed shot noise is evident in the constant values of spatial frequency amplitude at high spatial frequencies that is determined by the value of c_0 in the cosine expansion. In the case of SAX, we see that the cutoff spatial frequency for imaging depends on the noise level. As the noise level rapidly rises with higher SAX orders, the cutoff spatial frequency is reduced. These particular values of cutoff depend on the noise level in the measurement, which in turn follows the average value of the fluorescent emission. Thus, traditional SAX imaging is likely limited to bright objects. The dSAX method was also compared, which extracts the third-order nonlinear signal from the same saturated images used for CSA. The result is that with no noise present, both dSAX and the third harmonic from SAX yield nearly identical results. When noise is introduced, the dSAX method yields much higher SNR. Even though dSAX gives a much better SNR than SAX it still relies on the extraction of the third-order nonlinear signal, which suffers from the same

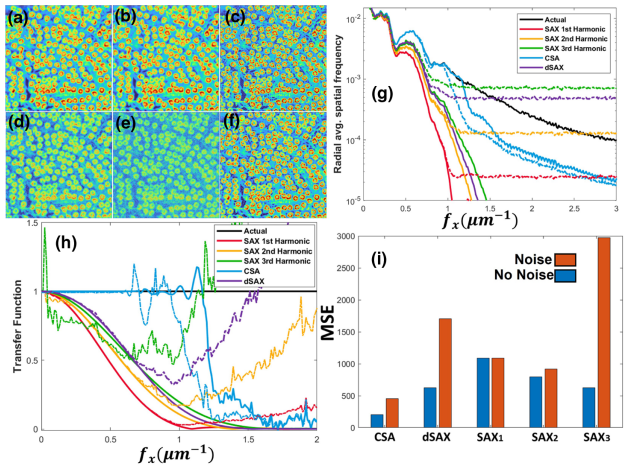

Fig. 5. (a) and (d) Simulations comparing the imaging performance of the dSAX; (b) and (e) SAX; and (c) and (f) CSA imaging techniques with and without noise. Images (a)–(c) show the reconstructions without noise and (d)–(f) with additive Gaussian noise and Poisson noise present in the simulated data (mean photon count of 25000 and additive Gaussian noise with standard deviation of 1% of the maximum value). (a) and (d) Reconstructed images using dSAX extracting the third-order nonlinear signal [10]. (b) and (e) Reconstructed images using SAX demodulated at the third harmonic. (c) and (f) CSA technique with a set of 15 images with the intensity going from .01 to $4I_{sat}$. The data is simulated with a nuclear pore complex image [15]. (g) Radial average of the spatial frequency content of the reconstructed images with each normalized to the DC value. (g) and (h) Solid lines indicate the reconstructions without noise present and the dashed lines represent reconstructions with noise present. (h) Transfer function of the reconstructed images. This is found by dividing the Fourier transform of the reconstructed image by the Fourier transform of the true image and then taking the radial average. Bar graph (i) shows the MSE of each of the reconstructions. SNR values were also calculated for CSA (23.3 dB), dSAX (18.1 dB), and SAX demodulated at the first through third harmonics (38.17 dB, 21.3 dB, and 8.7 dB).

multiplexed noise. While CSA is not subject to multiplexed noise, we see that the amplitude of the spatial frequency content is attenuated at high spatial frequencies when noise is present.

The quality of the estimated images can be quantified by computing the SNR with the formula $\mathrm{SNR} = 10\log_{10}[\sum_{i=1}^{N}\hat{X}_i/\sum_{i=1}^{N}(\hat{X}_i - X_i)]$ and the mean squared error (MSE) with the formula $\mathrm{MSE} = N^{-1}\sum_{i=1}^{N}(X_i - \hat{X}_i)^2$,

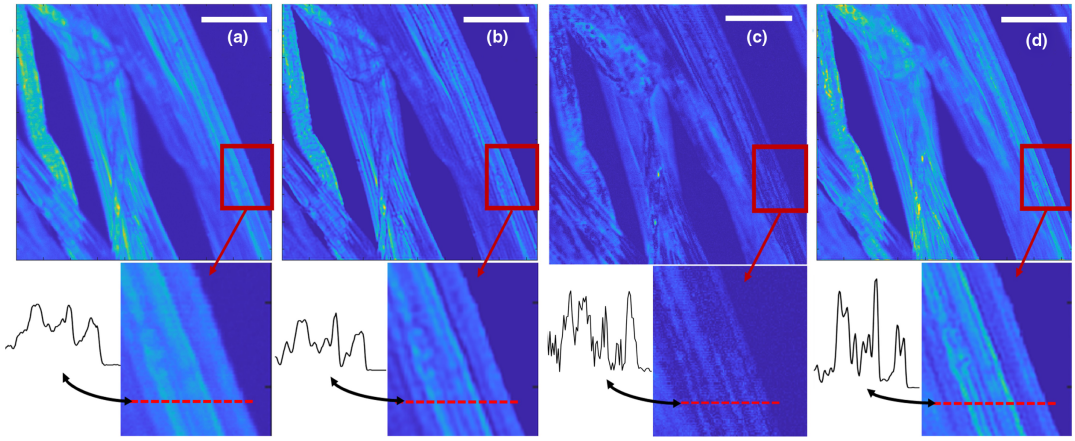

Fig. 6. (a) Laser scanned image with an input intensity of $0.29\alpha_0$. (b) Resultant deconvolution of the laser scanned image in (a) using FISTA. (c) Resultant image using dSAX [10]. (d) Resultant image using CSA with all four laser scanned images using FISTA. Below each image shows a zoomed-in portion of each corresponding reconstruction along with a line out. This clearly shows a resolution enhancement in the case of CSA since more fibers can be resolved. This is especially evident near the far-right edge of the fibers where only the CSA reconstruction can distinguish that there are two sub-resolution fibers that run parallel to each other along this edge. The dSAX image shows an improvement in resolution similar to the deconvolution, but the SNR is poor compared to the CSA image. Scale bar is 25 μm.

where N is the total number of elements, X is the true image, and $\hat{X}$ is the observed image. These formulae benefit from the fact that for the simulations the true object is known. Here, we see that the first-order SAX image, which is similar to a conventional LSM image, is robust to this particular level of noise. However, this first-order image has low spatial resolution compared to CSA and higher SAX orders. The second-order SAX image is mildly affected by the noise, whereas the third-order SAX image is severely degraded. The CSA image SNR and MSE are mildly degraded by the noise; however, the SNR is significantly higher and the MSE is significantly lower for the CSA image compared to all SAX image orders. Compared to dSAX, CSA also results in a higher SNR and spatial frequency content as observed in both the radial average of the spectrum and transfer function compared to the ground truth. While further study is required to fully explore the impact of noise, these conditions clearly show significant benefits for CSA imaging.

The experimental CSA images are shown in Fig. 6. The experiments were conducted with ∼250 fs pulses centered at 1035 nm (Y-Fi NOPA, Thorlabs Inc.). The peak saturation parameter $\alpha_{0,s}$ is controlled by varying the average power of the excitation beam with a constant amplitude RF driving signal applied to an acousto-optic modulation (AOM). The illumination beam is directed into a laser scanning nonlinear microscope [16]. For this experiment, two-photon absorption of fluorescein-dyed fibers was used. There is no change in the algorithm from linear absorption to two-photon absorption for the CSA and dSAX techniques. The only modification for CSA is to ensure the model for the saturated PSF is adapted to account for a slight change in the saturation function. This is described in detail in Section 6 in Supplement 1. The emitted two-photon fluorescence from the sample is collected in the forward direction with a photomultiplier tube (PMT) after being passed through a dichroic filter to reject the pump light. Saturation curves are measured by recording the PMT signal as a function of incident illumination power that is rapidly varied applying a ramp function to the RF modulation signal amplitude of the AOM, allowing for an accurate estimation of the PSF shape as intensity values reach different saturation levels.

The fluorophore is excited through two-photon absorption with the pulsed laser source. This excitation produces a saturation curve that is shown in Fig. S7 in Supplement 1. Accurate modeling of each saturated PSF requires that the saturation curve be well characterized. Measured fluorescent saturation data are fit to the pulsed two-photon excitation model given in Eq. (S16) in Supplement 1. The fit to the experimental data is used as the nonlinear function map that transforms the measured low intensity linear PSF to the ePSF at a given experimental saturation level to estimate the saturated ePSFs used in the super deconvolution process. The effective linear input PSF is estimated from an image of a 100 nm diameter fluorescent nanodiamond under conditions of weak (i.e., unsaturated) excitation. Saturated ePSFs for the super deconvolution model are synthesized from the saturation curve and the illumination PSF.

Images of the sample, composed of tissue fibers stained with fluorescein dye, were taken at four different power levels reaching a maximum peak saturation level three times the two-photon saturation intensity; i.e., $\alpha_0^{(2)} = 3$. These images were used to obtain a saturation curve by rapidly measuring the fluorescent signal with the excitation beam parked at one position in the sample. The measured fluorescent signal data points were fit to Eq. (S16), which expresses the mean fluorescence signal F for two-photon emission assuming the pulse duration is much shorter than the fluorescence lifetime and time between pulses, and $I_{\text{sat}}^{(2)}$ is the two-photon saturation intensity. With the saturation curve based on a fit to the experimental fluorescent power saturation curve, the CSA algorithm can be applied to the image data. The images are first aligned with a cross correlation to remove any spatial drift accumulated between the scans. The image alignment is performed by minimizing the cross-correlation amplitude between a selected reference image

and the remaining images in the stack. Then, a set of saturated ePSFs were computed using the experimentally derived linear PSF measurement and the two-photon saturation curve function. Both the images and the ePSFs are normalized to unity at their peak values and run through the CSA deconvolution algorithm, which is a FISTA optimization routine that is used to estimate a single, high-resolution image. The experimental reconstructed images are shown in Fig. 6. For comparison, Fig. 6(a) shows the LSM image for a relatively weak excitation at $\alpha_0^{(2)} = 0.29$. The simple deconvolution of this image shown in Fig. 6(b) shows that higher resolution features can be extracted from the two-photon fluorescence image of fluorescein-dyed fibers. A reconstructed image solving for the third-order nonlinear signal using the dSAX technique is shown in Fig. 6(c). A CSA image obtained from a set of four saturation levels with $\alpha_0^{(2)} = .29, .8807, 1.81, 2.98$ produces a higher resolution image with better SNR. For comparison, a zoomed in portion of each image is shown with plots of a line-out of a section of the image. This clearly shows a resolution enhancement afforded by the CSA technique shown in Fig. 6(d) with the CSA image resolving more fibers than the LSM, deconvolved or dSAX images. The LSM image shows a relatively high shot noise level. The dSAX image shows a nice improvement in resolution, but the SNR is quite low. Single linear deconvolution helps suppress this noise and brings out some of the high spatial frequency information in the image. CSA brings out more information than the linear convolution and dSAX across the spatial frequency band since it uses information from many orders of the nonlinear signal simultaneously, which highlights the improved imaging performance using CSA.

5. CONCLUSIONS

To summarize, we have introduced what we believe is a new super-resolution optical imaging modality in which we exploit information from a set of images, each acquired with a distinct ePSF. In this work, the set of ePSFs, each of which corresponds to a fluorescent image acquired at increasing levels of saturation of the fluorescent excitation, are jointly deconvolved to produce a super-resolution image. While the excitation of the fluorescent excited state is nonlinear in the case of saturation, we may define an effective PSF that follows a linear image formation model that is determined by the saturation curve of the excited fluorescent molecule. As the saturation level increases, these ePSFs become steeper, wider, and brighter. As a result, the eOTF exhibits both a higher SNR and higher spatial frequency support at higher saturation levels. We developed a computationally efficient strategy to jointly solve a super deconvolution problem by combining all the information represented in the spatial frequency diversity across the set of measured images with the set of ePSFs. This CSA strategy combines all the information acquired from the set of measurements. Each measurement spans a range of transverse spatial frequencies. The weakly saturated images have a narrower range of spatial frequency support, and thus exhibit higher SNRs in the image data at low transverse spatial frequencies. By contrast, the higher saturation level images have higher signals overall, but the signals are spread across a much broader spatial frequency range. The super deconvolution requires that the estimated image simultaneously satisfy all the measured image data. As a result, a high SNR at low spatial frequencies provided by images with low saturation helps to stabilize the higher spatial frequency content obtained with the saturated images. Consequently, CSA yields an improved spatial resolution as well as higher SNR images than is possible with conventional LSM, SAX, dSAX or even from the deconvolution of either LSM or SAX images. Moreover, Fig. 2 shows that the resolution improvements continue to scale as the peak saturation increases. Obviously, the improvements cannot scale indefinitely, but some fluorescent and luminescent systems can reach extremely high saturation levels while remaining well below any damage threshold. Indeed, even in the case of organic dyes that can tolerate GW/cm^2 peak intensity levels, $\alpha_0 \sim 3000$ is possible. In the case of systems with similar absorption cross sections, but long lifetimes, such as rare earth ions and photoswitchable proteins, the peak saturation level can exceed 10^5, suggesting extremely fine spatial resolution imaging is possible. There are two other limitations of this technique: its reliance on relatively high saturation levels, which can cause photobleaching or damage in some samples, and the requirement for precise knowledge of the system's PSF and the saturation function of the samples.

Funding. Chan Zuckerberg Initiative; U.S. Department of Energy (DE-SC0017200); National Science Foundation (1707287); National Institutes of Health (R21EB025389, R21MH117786).

Acknowledgment. J. Squier is supported by the NSF.

Disclosures. The authors declare no conflicts of interest.

Data availability. Data related to this paper are available at [17].

Supplemental document. See Supplement 1 for supporting content.

REFERENCES

1. "Beyond the diffraction limit," Nat. Photonics **3**, 361 (2009).
2. E. Betzig and J. K. Trautman, "Near-field optics: microscopy, spectroscopy, and surface modification beyond the diffraction limit," Science **257**, 189–195 (1992).
3. S. W. Hell, "Far-field optical nanoscopy," Science **316**, 1153–1158 (2007).
4. F. C. Zanacchi and A. Diaspro, "Fluorescence photoactivation localization microscopy," in *Encyclopedia of Biophysics* (Springer, 2013), pp. 812–814.
5. L. Schermelleh, R. Heintzmann, and H. Leonhardt, "A guide to super-resolution fluorescence microscopy," J. Cell Biol. **190**, 165–175 (2010).
6. S. W. Hell, R. Schmidt, and A. Egner, "Diffraction-unlimited three-dimensional optical nanoscopy with opposing lenses," Nat. Photonics **3**, 381–387 (2009).
7. L. von Diezmann, Y. Shechtman, and W. E. Moerner, "Three-dimensional localization of single molecules for super-resolution imaging and single-particle tracking," Chem. Rev. **117**, 7244–7275 (2017).
8. P. Wang, M. N. Slipchenko, J. Mitchell, C. Yang, E. O. Potma, X. Xu, and J.-X. Cheng, "Far-field imaging of non-fluorescent species with subdiffraction resolution," Nat. Photonics **7**, 449–453 (2013).
9. K. Fujita, M. Kobayashi, S. Kawano, M. Yamanaka, and S. Kawata, "High-resolution confocal microscopy by saturated excitation of fluorescence," Phys. Rev. Lett. **99**, 228105 (2007).
10. Y. Nawa, Y. Yonemaru, A. Kasai, R. Oketani, H. Hashimoto, N. I. Smith, and K. Fujita, "Saturated excitation microscopy using differential excitation for efficient detection of nonlinear fluorescence signals," APL Photon. **3**, 080805 (2018).

11. G. P. J. Laporte, N. Stasio, C. J. R. Sheppard, and D. Psaltis, "Resolution enhancement in nonlinear scanning microscopy through post-detection digital computation," Optica **1**, 455–460 (2014).
12. R. A. Bartels, G. Murray, J. Field, and J. Squier, "Super-resolution imaging by computationally fusing quantum and classical optical information," Intel. Comput. **2022**, 0003 (2022).
13. MicroscopyU, "Male rat kangaroo kidney epithelial cells (PtK2 line)," (1999), https://www.microscopyu.com/gallery-images/male-rat-kangaroo-kidney-epithelial-cells-ptk2-line-1.
14. N. Antipa, G. Kuo, R. Heckel, B. Mildenhall, E. Bostan, R. Ng, and L. Waller, "DiffuserCam: lensless single-exposure 3D imaging," Optica **5**, 1–9 (2018).
15. H. Ris, "High-resolution field-emission scanning electron microscopy of nuclear pore complex," Scanning **19**, 368–375 (1997).
16. M. D. Young, J. J. Field, K. E. Sheetz, R. A. Bartels, and J. Squier, "A pragmatic guide to multiphoton microscope design," Adv. Opt. Photon. **7**, 276–378 (2015).
17. G. Murray, P. A. Stockton, J. Field, A. Pezeshki, J. Squier, and R. A. Bartels, "SDI," GitHub (2023), https://github.com/RandyBartelsCSU/SDI.